Atomic electrostatic maps of point defects in MoS$_2$

Sebastian Calderon V.[†], Rafael V. Ferreira[†#], Deepyanti Taneja[‡], Jayanth Raghavendrarao T.[‡],

Langyan Zhou[‡], Ricardo M. Ribeiro[†⚕], Deji Akinwande[‡§], Paulo J. Ferreira[†§#]*

[†] INL – International Iberian Nanotechnology Laboratory, Av. Mestre José Veiga s/n, 4715-330 Braga, Portugal

[‡] Microelectronics Research Center, Department of Electrical and Computer Engineering, The University of Texas at Austin, Austin, Texas 78758, United States

[§] Materials Science and Engineering Program, The University of Texas at Austin, Austin, Texas 78712, United States

[⚕] Department and Centre of Physics, University of Minho, Campus of Gualtar, 4710-057, Braga, Portugal

[#] Mechanical Engineering Department and IDMEC, Instituto Superior Técnico, University of Lisbon, Av. Rovisco Pais, 1049-001 Lisboa, Portugal

Abstract

In this study, we use differential phase contrast images obtained by scanning transmission electron microscopy combined with computer simulations to map the atomic electrostatic fields of MoS_2 monolayers and investigate the effect of sulphur monovacancies and divancancies on the atomic electric field and total charge distribution. A significant redistribution of the electric field in the regions containing defects is observed, with a progressive decrease in the strength of the projected electric field for each sulphur atom removed from its position. The electric field strength at the sulphur monovacancy sites is reduced by approximately 50% and nearly vanishes at the divacancy sites, where it drops to around 15% of the original value, demonstrating the tendency of these defects to attract positively charged ions or particles. In addition, the absence of the sulphur atoms leads to an inversion in the polarity of the total charge distribution in these regions.

Introduction

Molybdenum disulphide (MoS_2) is a widely studied transition metal dichalcogenide with a layered structure, each layer consisting of a sheet of molybdenum (Mo) atoms arranged in a close-packed configuration, enclosed by two sheets of sulphur (S), also in a close-packed configuration. This material is particularly interesting in monolayer form because it exhibits a direct bandgap, thus presenting high potential for use in flexible electronics and photodetectors [1–4]. Nonetheless, the production of monolayers at large scales is still a matter of research and their quality is usually affected by structural defects, such as point defects, dislocations and grain boundaries. Yet, a fundamental understanding regarding the influence of these specific defects on the properties is still lacking, in particular with respect to electronic transport, single-photon excitation and trapping of adatoms. This is critical to design and synthesize materials with controlled properties, which is even more relevant for 2D materials, since any defect will have a significant presence in their thin structure. In particular, for MoS_2 monolayers, the presence of defects may be responsible for significant variations in their electronic and optical properties.

In the case of exfoliated MoS_2 monolayers, different types of defects are commonly reported, including sulphur monovacancies, sulphur divacancies, vacancy complexes composed of a missing Mo atom along with the three surrounding S atoms in one or both of the encapsulating planes, as well as antisite defects of Mo substituting an S_2 or vice versa. Among these defects, the sulphur mono- and divacancies are the most common, due to their lower energy of formation when compared to other types of defects [5,6].

3

These defects can be observed at the atomic scale by scanning transmission electron microscopy (STEM), which can unambiguously distinguish a sulphur monovacancy from a divacancy or an antisite defect. This extraordinary ability to probe materials at the atomic level can be also coupled with electron energy loss spectroscopy (EELS) to study their electronic structure. However, the acquisition of EELS maps in 2D materials is extremely challenging due to the instability of these type of structures under the electron beam, especially in defected regions. For the case of MoS_2, sample degradation can occur not only at high accelerating voltages, by knock-on damage, but also at lower voltages, by means of radiolysis [7]. Hence, creating a 2D map of bonding states in these materials, particularly in the presence of point defects, is still quite challenging.

In this context, to obtain information beyond the structural characteristics of MoS_2, use of the differential phase contrast (DPC) STEM techniques at atomic resolution is proposed. These techniques have proven to be a powerful resource for acquiring information about the projected atomic electrostatic field and total charge distribution in materials, convolved with the electron intensity distribution of the STEM probe or, more precisely, with the contrast transfer function [8], revealing details about chemical bonding, in a way no other technique has permitted [9–11]. This information is retrieved by measuring the centre of mass (CoM) of the intensity distribution in convergent-beam electron diffraction (CBED) patterns, using a position-sensitive detector. This can be achieved by using either a segmented or pixelated detector to collect the diffraction disk intensity distribution. However, one general limitation is that very thin samples are required, so that dynamical diffraction effects are avoided. In the case of segmented detectors, quantification capability is less accurate compared to that of a pixelated detector, due to large parts of the diffraction disk being averaged [9]. Nonetheless, the speed and sensitivity of

segmented detectors have prevailed and have been used to obtain remarkable information about the electrostatic field and charge distribution in materials such as GaN [10], graphene [11], hexagonal boron nitride [12], monolayer transition metal dichalcogenides such as MoS_2 and WS_2 [13], as well as to image light and heavy elements simultaneously [14,15].

This report describes the application of the DPC-STEM techniques to an investigation of the electrostatic features of MoS_2 in the vicinity of defects. In particular, electrostatic maps of pristine regions and areas containing the presence of sulphur vacancies were recorded at 60 kV and 200 kV, supported by multislice computer simulations. Under these conditions, we were able to visualise in MoS_2, the experimental atomic-level force field in regions containing defects. These observations should be an important contribution to understanding the influence carried by defects investigated on the electronic properties of MoS_2 – particularly as it relates to adatom trapping – along with the mechanisms by which their action occurs.

Results and Discussion

In this work, we take advantage of the fact that MoS_2 monolayers do not cause significant dynamical scattering of the electron beam to collect atomic electrostatic field information in pristine and defect-containing regions of this material. In order to account for the aforementioned accuracy-loss in the measurement of the electric field magnitude and direction, when using segmented detectors, multislice computer simulations of 4D-STEM images were carried out, using the same configuration as the one employed experimentally. Analysis of the results shows that the electric field magnitudes obtained from segmented detectors are overestimated in comparison to those obtained from the full diffraction disk, with the largest absolute differences appearing where the field is strongest. However, relatively speaking, it is in the interatomic and

low-field regions that the increase in magnitude is the highest, by factors reaching about three times. Similarly, errors in the direction of the electric field are most significant in the low-field regions, occurring near the centre of the hexagonal pattern of MoS_2. Generally, as expected, the highest measurement error is found at the regions where the electric field is lowest since the small deflection of the electrons in these areas is not fully captured by the annular detector (Supporting Information Figure S1). Despite these considerations, observations regarding the field magnitude suggest that a qualitative analysis of this parameter is possible using a segmented detector. It is worth noting, however, that the trend observed indicates that larger multiplicative factors would be expected for fields smaller than those considered in the simulations.

Figure 1a shows an optical image of the sample investigated, a large flake of exfoliated MoS_2 transferred onto a SiN ultra-flat grid. Raman spectra (Figure 1b) were collected throughout the sample to help with the identification of regions of monolayer MoS_2. The spectrum from the area enclosed by the white rectangle in Figure 1a revealed the E_{2g} and A_{1g} vibrations modes of MoS_2, which are sensitive to the flake thickness, allowing an accurate determination up to 4 monolayers based on the peak separation [16]. The separation of the E_{2g} and A_{1g} peaks is approximately 19.7 cm^{-1}, which is attributed to regions with a mixture of mono- and bilayer MoS_2. These locations were then observed by annular dark field (ADF) STEM at 60 kV (Figures 1c), which confirmed the existence of regions of monolayer MoS_2 (inset in Figure 1c). Figure 1d shows an image resulting from a series acquisition of 50 fast-scanning ADF-STEM images (5 µs/pixel) recorded in this monolayer region, which were aligned and then averaged via cross-correlation. The Mo (brighter spots) and S sites can be clearly identified in Figure 1d, while the FFT (inset) shows the diffraction pattern characteristic of a single layer of MoS_2.
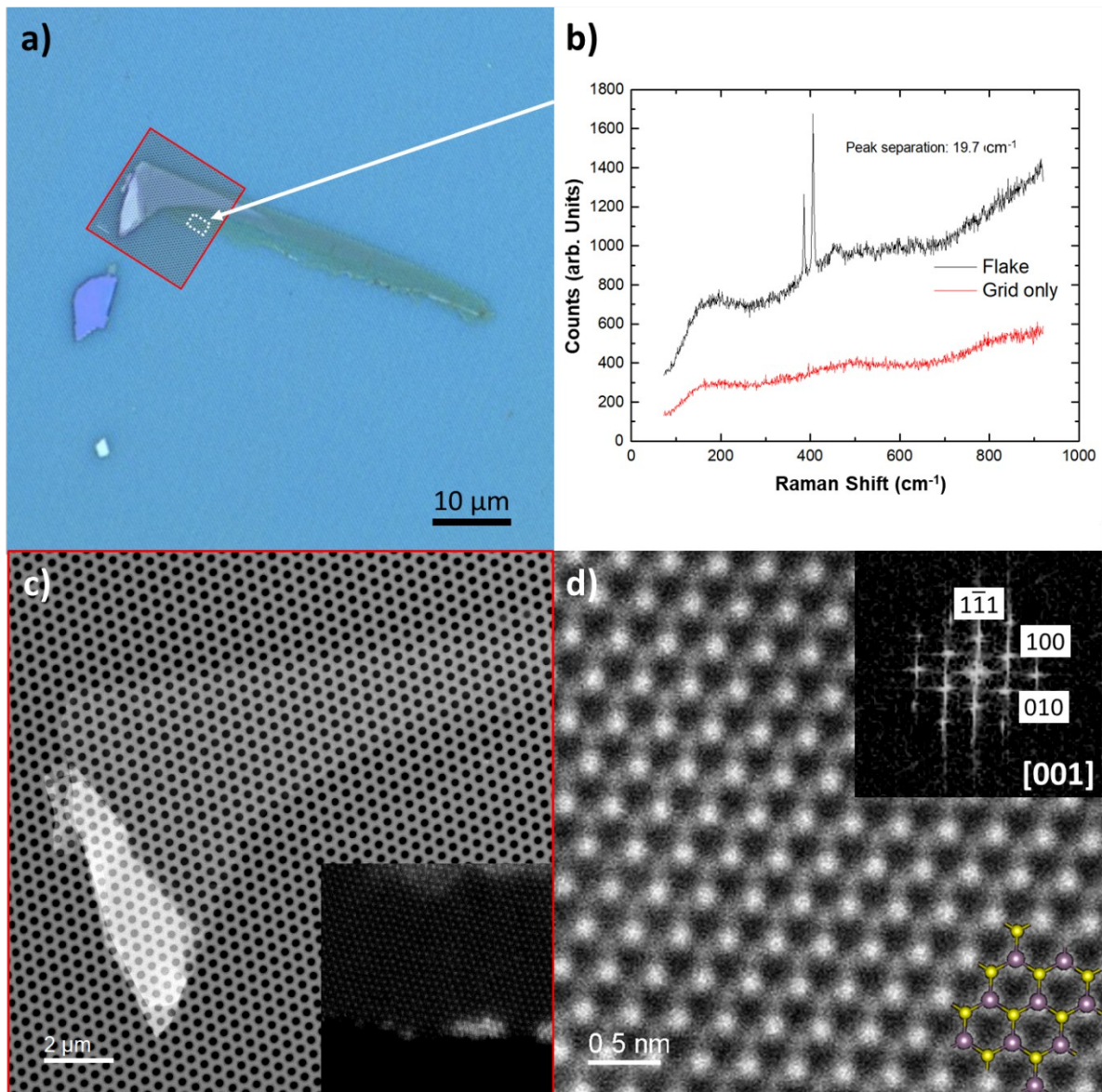
Figure 1. a) Optical image of exfoliated MoS_2 transferred onto a SiN ultra-flat grid, b) Raman spectra collected in the white rectangle and on the grid only, c) ADF-STEM image of the exfoliated MoS_2 shown within the red square in a). The inset in c) represents an ADF-STEM image of monolayer MoS_2 collected within the regions identified as such by Raman spectroscopy. d) Stack of 50 fast-scanning ADF-STEM images from a MoS_2 monolayer, with the FFT shown in the inset at the upper right corner, revealing the diffraction pattern characteristic of

monolayer MoS_2. The inset at the bottom right represents the MoS_2 atomic model with purple Mo and yellow S atoms. All the STEM images were acquired at 60 kV.

To obtain both structural information and the projected electric field (eDPC), charge distribution (dDPC) and potential (iDPC) from pristine regions of material, a series of 7–10 images were acquired at 60 kV using the ADF and the segmented detectors simultaneously (Figure 2). This image series allows us to obtain a higher signal-to-noise ratio and consequently improve the interpretability of the results, which show a good match with DPC images that were simulated using the experimental conditions (insets in Figure 2).

Figure 2a shows the atomic model of MoS_2, which has been tilted slightly off-axis to observe both of the overlapping S atoms. The ADF-STEM image shown in Figure 2b is quite clear in identifying the Mo atoms (brighter) and the two overlapping S atoms (darker), thus revealing the projected hexagonal symmetry created with the atomic configuration of MoS_2. In addition, the projected potential (Figure 2c), electric field (Figures 2d and 2e) and charge distribution (Figure 2f) also show a hexagonal symmetry. It is worth noticing that the projected potential (Figure 2c) is missing some of the mass-thickness information that is observed in the contrast of ADF-STEM images, making it more difficult to differentiate between the Mo and S atomic columns and stressing the importance of the simultaneous acquisition of ADF-STEM and DPC-STEM images. The dashed red line highlights the hexagonal symmetry, where the electric field (Figure 2d) reaches its minimum in the centre of the hexagons formed by the three Mo atoms and six S atoms in projection (yellow arrow), while local minima are observed between the Mo-S bonds (green arrow), due to cancellation of the opposite electric fields originating from each atom. Figure 2e shows a mapping of the electric field, where the colours point to the orientation of the

electric field using as reference the center of the colour wheel (inset) and the luminosity indicates the magnitude. The charge distribution (Figure 2f), on the other hand, shows positively charged atomic columns surrounded by neutral regions (white), which decrease towards a negative charge distribution at the centre of the hexagons.

The images obtained in pristine regions of the sample indicate that it is possible to determine the electric field and charge distribution with sub-nanometre spatial resolution. However, the collection of image series is hindered in the presence of defects due to the instability of such areas under the electron beam, and thus only single-frame collection is possible. A comparison between single-frame DPC images acquired at 200 kV and 60 kV is shown in the Supporting Information (Figure S2). The images clearly demonstrate that to be able to obtain detailed information about the electric field and charge distribution, higher resolution single-frame images are required, and therefore, in addition to 60 kV images, higher resolution images were obtained at 200 kV. Indeed, Shibata et al. [11] previously pointed out that electric field imaging requires a higher resolution than conventional ADF imaging. Furthermore, by increasing the acceleration voltage it is also possible to decrease the probe size and thus, reduce the effect of the probe on the quantification of the electric field, as demonstrated later using image simulations.
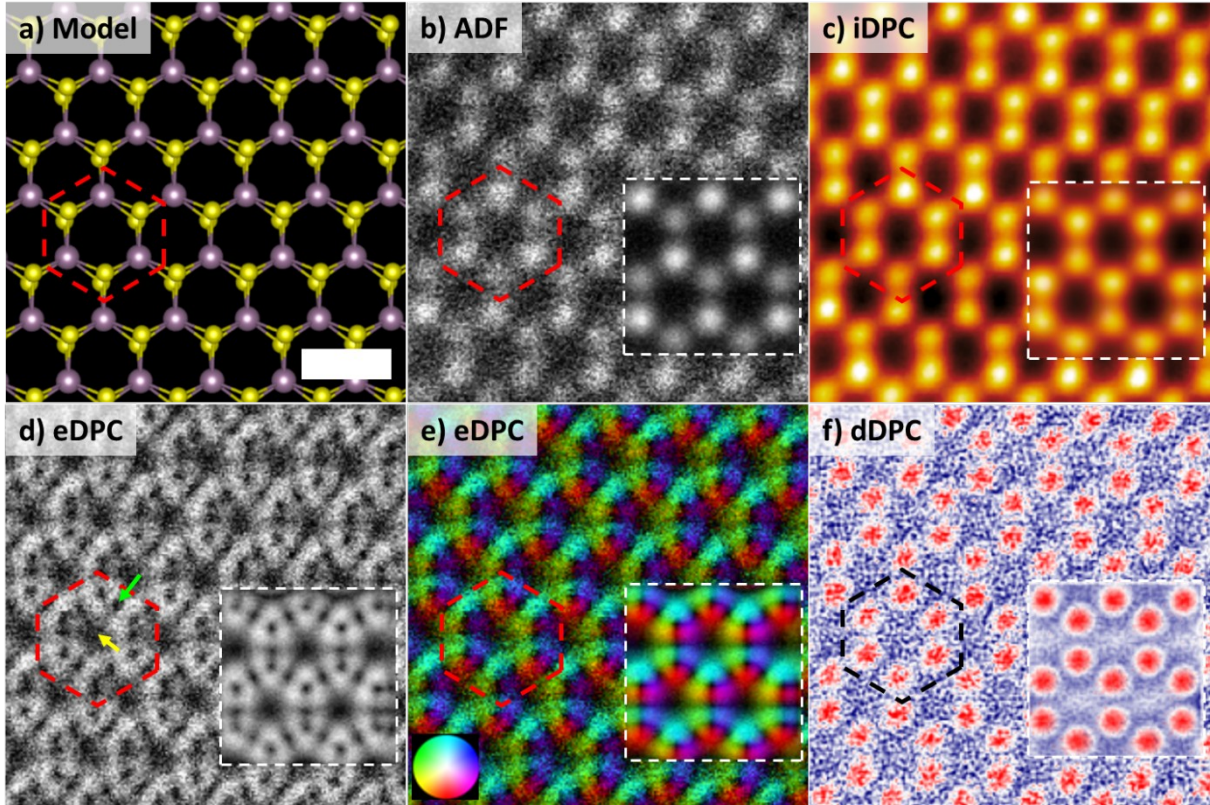
Figure 2. a) Atomic model of MoS_2, tilted slightly off-axis to observe the two S atoms located on top of each other. Stack of 10 fast-scanning images from a MoS_2 monolayer: b) ADF-STEM, c) integrated DPC signal, proportional to the projected potential; d) eDPC image, proportional to the projected electric field; e) electrostatic map for the projected electric field in d), where the inset colour wheel indicates the orientation (colour) and strength (luminosity) of the electric field; f) dDPC image, proportional to the projected charge distribution. The inset images correspond to multislice simulation images for MoS_2. The scale bar in image a) corresponds to 4 Å.

In order to create regions with defects, the 200 kV electron beam was employed to achieve a frame-by-frame dose increase that could be partially controlled by changing the pixel size and dwell-time during acquisition. Komsa et al. [17] have calculated that the minimum kinetic

energy required to sputter an atom from MoS_2 is around 90 keV. However, they have also demonstrated that in the presence of a vacancy the displacement of a S atom can occur at 80 keV. Additionally, radiolysis can also produce defects at lower voltages, though at much slower rates, as shown by Zhou et al. [7].

Figure 3 shows a comparison between a pristine region of MoS_2 (Figure 3a) and two others containing defects, namely a single sulphur vacancy (Figure 3b) and a sulphur divacancy (Figure 3c). As displayed in Figure 3, all the experimental images show a very good agreement with their simulated counterparts. The sulphur mono- and divacancy sites can be clearly identified in the ADF and iDPC images by a progressive loss of contrast, as would be expected. The eDPC images offer information about the electrostatic force field at the atomic level. A careful examination of the eDPC images in the pristine areas shows that the electric field in the atomic sites points outwards, while the opposite situation is observed at the centre of the hexagons. The existence of vacancies in MoS_2 significantly modifies the distribution of the electric field. In particular, the presence of a single S vacancy (Figure 3b) reduces the magnitude of the projected field surrounding the atomic position; while in the presence of a sulphur divacancy, the electric field flips direction when compared to a pristine atomic site. The dDPC images, which show the projected charge distributions, confirm these findings. In fact, in pristine samples, a positive charge distribution is observed in the S position, which changes towards a negative charge distribution when a sulphur divacancy is introduced. The dDPC images show then how the absence of S atoms reduces the positive charge in the point-defect site to a more neutral charging state, ultimately flipping into a slightly negative region.

These results have strong implications with respect to the properties of MoS_2, in particular as it relates to the force field experienced by adatoms on its surface. Specifically, the aforementioned

inversion of the electric field direction at the centre of the hexagons and, to an even greater extent, the magnitude reduction by 70 –85% brought upon by the creation of S vacancies, as demonstrated below, could play a critical role in the adsorption of impurities. In other words, the regions exhibiting the presence of vacancies may act as Coulomb traps, thus facilitating the adsorption of positively charged atomic species. For example, recent studies on the adsorption of Au ions in MoS_2 for non-volatile resistive switching [18] have shown that Au/Au^{+1} ions have a lower energy barrier compared to Au^{-1} for transitioning from a pristine region to the vacancy site, which is strongly correlated with the electric field determined in this report. In addition, this type of behaviour has been reported for graphene [11], which has exhibited the adsorption of anions and cations on its surface.
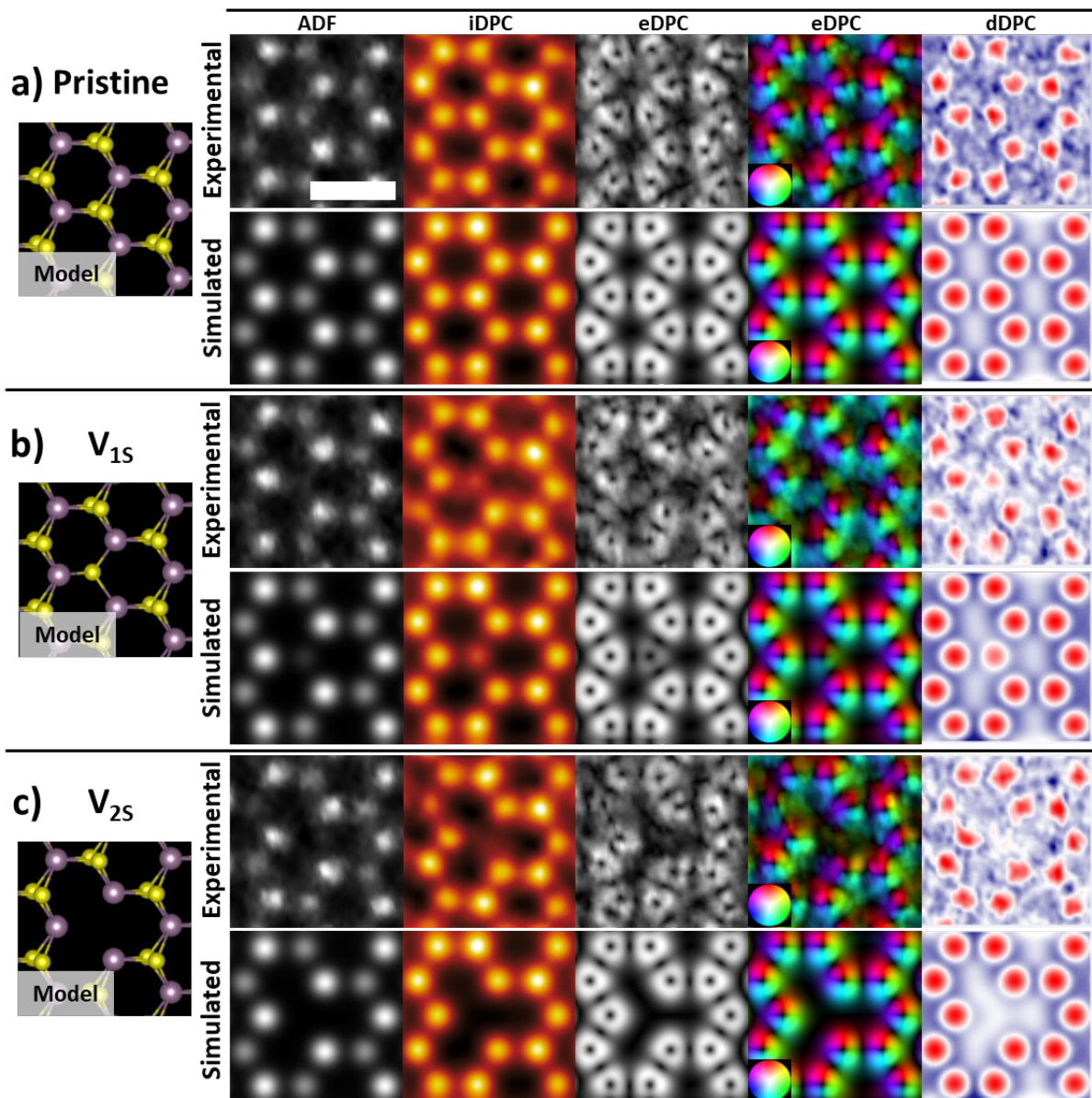
Figure 3. Experimental and simulated ADF-STEM and DPC-STEM images of a) pristine MoS_2 monolayer, b) MoS_2 monolayer with a single S vacancy (V_{1S}) and c) MoS_2 monolayer with a double S vacancy (V_{2S}). The scale bar in the pristine experimental ADF-STEM image corresponds to 4 Å.

In order to have a sense of the magnitude of the projected electric field and charge distribution, 4D-STEM simulations were carried out to be compared with the experimental results. Figure 4

shows the atomic electric field using an intensity map overlaid with a vector map, which indicates the magnitude and direction of the field, respectively. A simpler vector map representation is shown in Figure S3 of the Supporting Information. The projected electric field magnitude retrieved from the 4D-STEM simulations in the pristine region shows a maximum of approximately 210 V in close proximity to the atoms, reaching the absolute minimum in the centre of the hexagons. Similarly, DFT calculations convolved with the probe intensity distribution show very similar field magnitudes, with a maximum electric field value of 240 V, as shown in Figure 4c. As mentioned before, the electric field reaches a local minimum in between the Mo and 2S sites due to their opposite electric fields. As a single S vacancy is created, the local minima initially decrease, shifting slightly in the direction of the remaining S atom. Removing the second S atom then causes the minima to move and combine at the centre of the vacancy, where the electric field vanishes. The shifts of the electric field minima can be clearly observed in Figure 4, where points of minimum magnitude are indicated by the blue arrows.

In general, the electric field surrounding the sulphur site decreases in magnitude as the divacancy is formed, turning the region progressively more negatively charged when compared with the pristine material. It is worth noting that the electric field and the charge distribution results are blurred by the effective source size of the electron probe. Thus, convolution with the probe leads to a reduction of the real electric field magnitude. Hence, the smaller the probe, the better is the approximation to a non-convoluted electric field, as shown in the Supporting Information (Figure S4). To account for this effect, the 4D-STEM simulations in Figure 4 were convolved with a probe size of 80 pm (FWHM), based on the experimental value, which was calculated to be in the range of 80–85 pm.
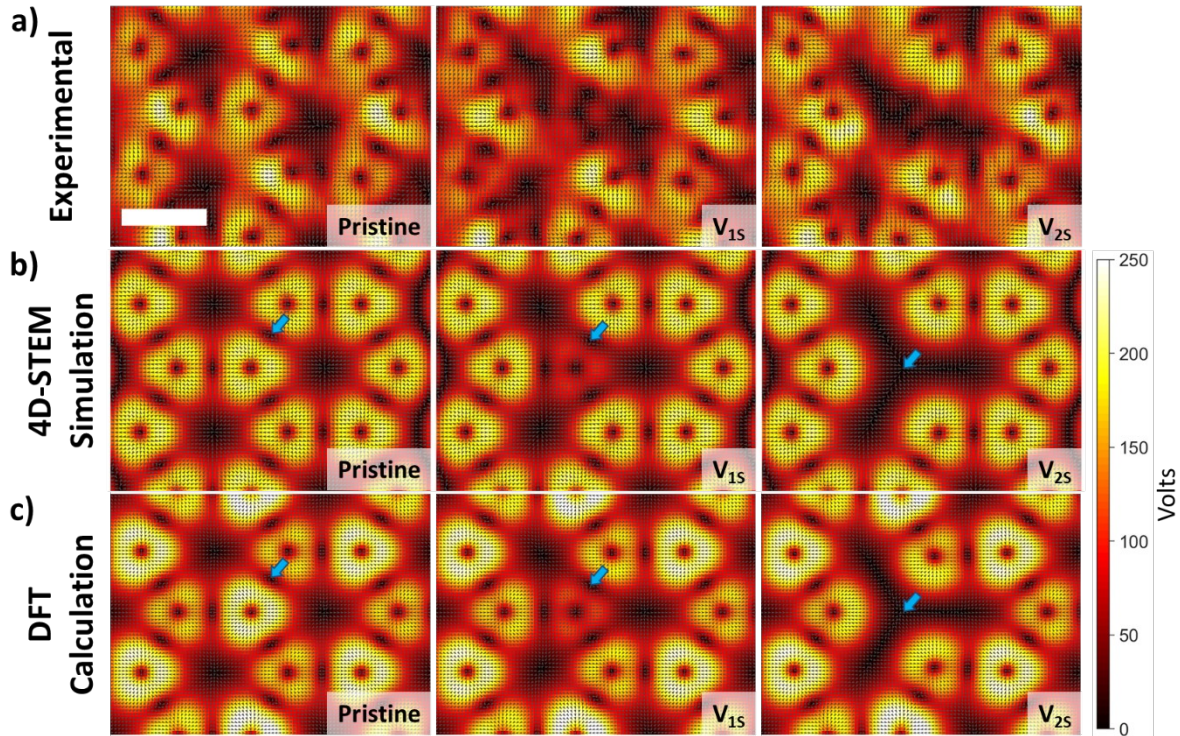
Figure 4. Representation of the projected atomic electric field using an intensity map overlaid with a vector map (one arrow per pixel), indicating the magnitude and direction of the field calculated from a) experimental averaged images from 6 frames of each defect type, b) 4D-STEM computer image simulations convolved with a probe size of 80 pm (FWHM), c) DFT calculations also convolved with the same probe. The scale bar in the pristine experimental image corresponds to 2 Å and the colour bar corresponds to the images in b) and c).

A comparison between the experimental and simulated electric field profiles in the defect region is shown in Figure 5. Figure 5a shows normalized electric field intensity profiles for correlated pristine, V_{1S} and V_{2S} regions, taken along the green arrow highlighted in Figure 5b, which demonstrate a very good agreement between the experimental and theoretical images obtained by both 4D-STEM simulations and DFT calculations. To compare the overall electric field configurations in each map of Figure 4, the projected electric field was integrated within the

region delineated by the blue triangle in Figure 5b. The results indicate a reduction of the experimental projected electric field at the single S vacancy sites to approximately 45.7% of the initial value, compared to a value of 44.6% and 44.7 % for 4D-STEM simulations and DFT calculations, respectively. In the case of the S divacancy sites, the projected electric field determined experimentally fades to nearly 30% of the initial value, whereas image simulations show a decrease to about 16% and 19% for the 4D-STEM and DFT images, respectively. Based on these results, and the fact that DFT calculations do not show accumulation of charges in the defected region, the difference in the magnitude in the divacancies site for the simulated and experimental results is attributed to the signal to noise ratio, which significantly affects the image quantification in the absence of any atom.
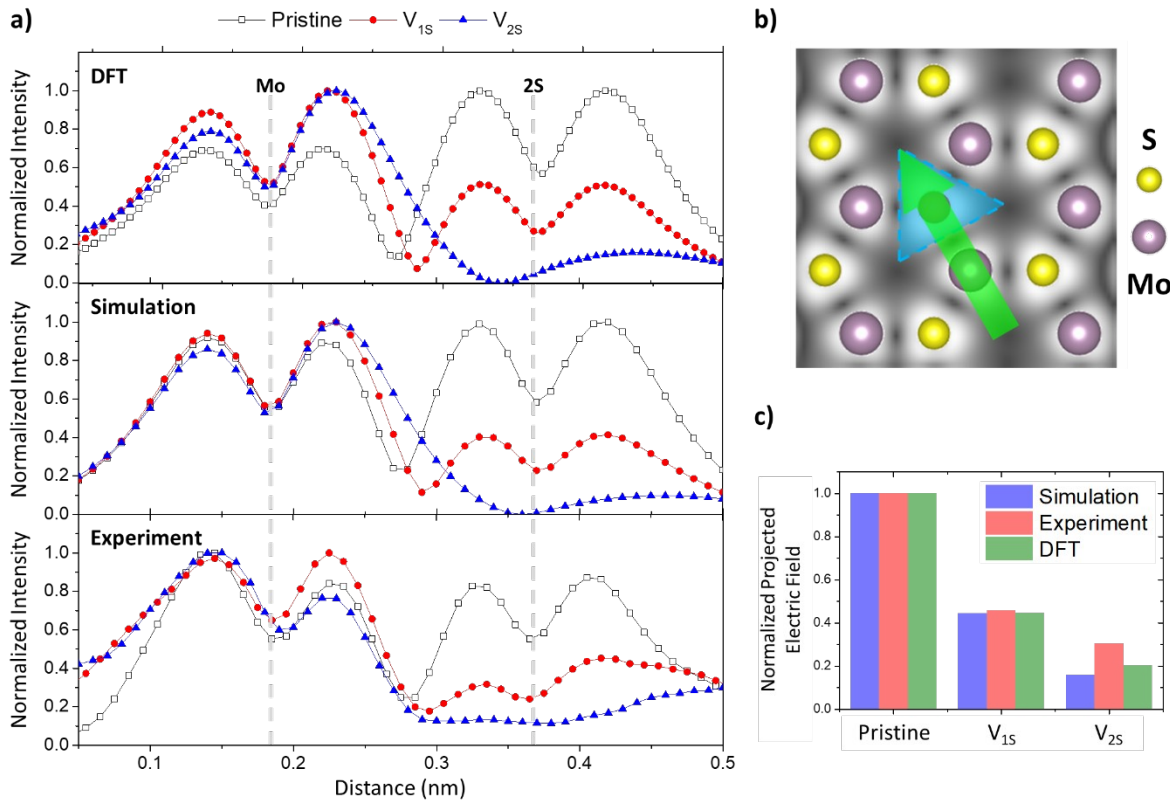
Figure 5. a) Normalized electric field intensity profiles in pristine, V_{1S} and V_{2S} regions of the DFT calculations, 4D-STEM simulations and experimental images shown in Figure 4, b) structural model of MoS_2 superimposed over the projected electric field, where the green arrow indicates the region where the line profiles were taken and the blue triangle contains the area in which the projected electric field was integrated, c) normalized projected electric field integrated over the blue triangle area shown in b), where the pristine region images are used as the references for normalization.

Concluding Remarks

In summary, we have demonstrated the capacity of DPC-STEM images to map the atomic-level electrostatic field in monolayer MoS_2, providing information about the local chemical state of monolayer MoS_2 in the presence of S vacancies. The results offer a sub-nanometre resolution that allows a detailed characterisation of the total charge distribution and of the intensity and direction of the electric field at the S atomic positions. Such information can be utilised to identify preferential locations for ion trapping or extended to force-field-bounded paths for adatom diffusion and adsorption. In fact, these results help to understand recent findings by Saban M. Hus et al. [19] on non-volatile single-switching using single defects, where S vacancies showed the capacity to serve as preferential local points for reversible adsorption of metal ions. In particular, the more negatively charged S divacancy regions could serve as ion traps, leading to the adsorption of the ions, which may result in a conducting local density of states and the reduced resistivity of the atomic sheet.

Experimental detail

Bulk crystals of MoS_2 were acquired through 2D Semiconductors. The samples were prepared by mechanical exfoliation of the parent crystals, enabled by the weak van der Waals coupling between the individual layers. The dry transfer technique consisted of employing a polydimethylsiloxane/polypropylene carbonate (PDMS/PPC) stamp to pick up the flake from the host substrate, using a combination of pressure and heat, followed by the drop-off of the flake together with the PPC on the TEM grid at a higher substrate temperature [20]. The PPC was subsequently washed off in acetone and isopropyl alcohol, and the sample was vacuum annealed to remove any residues. The successful transfer of monolayer flakes onto the TEM grids was confirmed using Raman and photoluminescence spectroscopy.

The ADF-STEM images were acquired on a double-corrected FEI Titan Themis operated at 60 kV and 200 kV, using a STEM probe current below 30 pA. The operation at 60 kV was used to image monolayers of MoS_2 below the knock-on damage threshold voltage. The accelerating voltage of 200 kV was used to generate point defects in the samples and to acquire higher resolution images. The images were recorded using convergence angles of 30 mrad at 60 kV and 21 mrad at 200 kV, with a pixel dwell time of 2–10 μs.

The DPC images were acquired using a four-segment annular detector (DF4), coupled to the same double-corrected FEI Titan-Themis microscope operated at 60 kV and 200 kV, using a STEM probe current below 30 pA. Images from individual segments were acquired with a pixel dwell time set at 2–10 μs using a 228 mm camera length, resulting in acceptance angles between 9 and 51 mrad, while when collecting the signal from the DF4 and ADF detectors simultaneously, the acceptance angles were limited to 9–36 mrad and 36–176 mrad, respectively. The DPC-STEM techniques were used to image the in-plane displacement of the transmitted electrons, while the images approximately proportional to the projected potential (iDPC-STEM),

the projected electric field (eDPC-STEM) and the projected charge distribution (dDPC-STEM) were calculated according to references [9,21–23]. Poisson noise was removed using the PureDenoise algorithm [24].

ADF-STEM and DPC-STEM images simulations were carried out using Dr. Probe V1.9 software package [25], considering the 2H staking order of MoS_2, based on the structure of the bulk single crystal. The thickness of the model varied from 0 to 13 nm. A single frozen-lattice configuration was used and the simulations were carried out using the experimental conditions at 60 kV and 200 kV. The images were convolved with a probe size of 0.8 nm to account for partial spatial coherence of the probe.

For the density functional theory (DFT) calculations, a 5x5 supercell was used to avoid interactions between defects in different images, as well as a vacuum of 29 r_{Bohr} in the direction perpendicular to the material. The first and second neighbours of the defects were allowed to relax in order to attain the equilibrium structure with defects. We used the software package Quantum ESPRESSO [26] with full relativistic, projector augmented wave (PAW) pseudopotentials [27], and the generalized gradient approximation of Perdew-Burke-Ernzerhof (GGA-PBE) [28]. The plane-wave cut-off was 60 Ry. The results were convolved with a probe size of 80 pm to compare with the STEM images.

ASSOCIATED CONTENT

Supporting Information. Maps for error analysis of electric field magnitude and angle determination; additional experimental and simulated electrostatic maps for accelerating voltages of 200 kV and 60 kV; experimental and simulated electric field maps in alternative representation; simulated electric field maps convolved with probes of different sizes.

The following files are available free of charge.

Maps for error analysis of electric field magnitude and angle determination; additional

experimental and simulated electrostatic maps for accelerating voltages of 200 kV and 60 kV;

experimental and simulated electric field maps in alternative representation; simulated electric

field maps convolved with probes of different sizes (PDF)

AUTHOR INFORMATION

Corresponding Author
*E-mail: paulo.ferreira@inl.int.

Author Contributions
S.C.V. conceived and planned the experiments, conducted the ADF- and DPC-STEM

measurements, analysed and treated the experimental images, performed the multislice image

simulations, and wrote the manuscript. R.V.F. performed the data processing and representation

in electrostatic maps with support from S.C.V., and assisted in the writing of the manuscript.

D.T. developed the glovebox transfer setup. Under the supervision of D.T., J.R.T. and L.Z.

performed the glovebox transfer of MoS_2 flakes to TEM grids, and the Raman and

photoluminescence spectroscopy measurements. R.M.R performed the DFT calculations. D.A.

and P.J.F. supervised the research. All authors discussed the results, revised and edited the

manuscript, and have given approval to the final version.

Notes
The authors declare no competing financial interest.

ACKNOWLEDGMENTS

REFERENCES

[1]   R. Ge, X. Wu, M. Kim, J. Shi, S. Sonde, L. Tao, Y. Zhang, J.C. Lee, D. Akinwande. Atomristor: Nonvolatile Resistance Switching in Atomic Sheets of Transition Metal Dichalcogenides. Nano Lett. 18(1) (2018), 434–441. doi:10.1021/acs.nanolett.7b04342.

[2]   M. Kim, R. Ge, X. Wu, X. Lan, J. Tice, J.C. Lee, D. Akinwande. Zero-static power radio-frequency switches based on MoS_2 atomristors. Nat. Commun. 9 (2018), 2524. doi:10.1038/s41467-018-04934-x.

[3]   D. Akinwande, N. Petrone, J. Hone. Two-dimensional flexible nanoelectronics. Nat. Commun. 5 (2014), 5678. doi:10.1038/ncomms6678.

[4]   M.D. Siao, W.C. Shen, R.S. Chen, Z.W. Chang, M.C. Shih, Y.P. Chiu, C.-M. Cheng. Two-dimensional electronic transport and surface electron accumulation in MoS_2. Nat. Commun. 9 (2018), 1442. doi:10.1038/s41467-018-03824-6.

[5]   D. Liu, Y. Guo, L. Fang, J. Robertson. Sulfur vacancies in monolayer MoS_2 and its electrical contacts. Appl. Phys. Lett. 103 (2013), 183113. doi:10.1063/1.4824893.

[6]   N.C. Frey, D. Akinwande, D. Jariwala, V.B. Shenoy. Machine Learning-Enabled Design of Point Defects in 2D Materials for Quantum and Neuromorphic Information Processing. ACS Nano. 14(10) (2020), 13406–13417. doi:10.1021/acsnano.0c05267.

[7]   W. Zhou, X. Zou, S. Najmaei, Z. Liu, Y. Shi, J. Kong, J. Lou, P.M. Ajayan, B.I. Yakobson, J.-C. Idrobo. Intrinsic Structural Defects in Monolayer Molybdenum Disulfide. Nano Lett. 13(6) (2013), 2615–2622. doi:10.1021/nl4007479.

[8]   E. Yücelen, I. Lazić, E.G.T. Bosch. Phase contrast scanning transmission electron microscopy imaging of light and heavy atoms at the limit of contrast and resolution. Sci. Rep. 8 (2018), 2676. doi:10.1038/s41598-018-20377-2.

[9]   K. Müller-Caspary, F.F. Krause, F. Winkler, A. Béché, J. Verbeeck, S. Van Aert, A. Rosenauer. Comparison of first moment STEM with conventional differential phase contrast and the dependence on electron dose. Ultramicroscopy 203 (2019), 95–104. doi:10.1016/j.ultramic.2018.12.018.

[10]   G. Sánchez-Santolino, N.R. Lugg, T. Seki, R. Ishikawa, S.D. Findlay, Y. Kohno, Y. Kanitani, S. Tanaka, S. Tomiya, Y. Ikuhara. Probing the Internal Atomic Charge Density Distributions in Real Space. ACS Nano 12(9) (2018), 8875–8881. doi:10.1021/acsnano.8b03712.

[11]   R. Ishikawa, S.D. Findlay, T. Seki, G. Sánchez-Santolino, Y. Ikuhara, N. Shibata, Y. Kohno. Direct electric field imaging of graphene defects. Nat. Commun. 9 (2018), 3878. doi:10.1038/s41467-018-06387-8.

[12]   O. Cretu, A. Ishizuka, K. Yanagisawa, K. Ishizuka, K. Kimoto. Atomic-Scale Electrical Field Mapping of Hexagonal Boron Nitride Defects. ACS Nano 15(3) (2021), 5316–5321. doi:10.1021/acsnano.0c10849.

[13]   S. Fang, Y. Wen, C.S. Allen, C. Ophus, G.G.D. Han, A.I. Kirkland, E. Kaxiras, J.H. Warner. Atomic electrostatic maps of 1D channels in 2D semiconductors using 4D scanning transmission electron microscopy. Nat. Commun. 10 (2019), 1127. doi:10.1038/s41467-019-08904-9.

[14]   I. Lazić, E.G.T. Bosch. Analytical review of Direct STEM Imaging Techniques for Thin Samples. Advances in Imaging and Electron Physics 199 (2017), 75–184. doi:10.1016/bs.aiep.2017.01.006.

[15]   S. de Graaf, J. Momand, C. Mitterbauer, S. Lazar, B.J. Kooi. Resolving hydrogen atoms at metal-metal hydride interfaces. Sci. Adv. 6(5) (2020). doi:10.1126/sciadv.aay4312.

[16]   C. Lee, H. Yan, L.E. Brus, T.F. Heinz, J. Hone, S. Ryu. Anomalous Lattice Vibrations of Single- and Few-Layer MoS_2. ACS Nano. 4(5) (2010), 2695–2700. doi:10.1021/nn1003937.

[17]   H.-P. Komsa, J. Kotakoski, S. Kurasch, O. Lehtinen, U. Kaiser, A. V. Krasheninnikov. Two-Dimensional Transition Metal Dichalcogenides under Electron Irradiation: Defect

Production and Doping. Phys. Rev. Lett. 109 (2012), 035503. doi:10.1103/PhysRevLett.109.035503.

[18]   R. Ge, X. Wu, L. Liang, S.M. Hus, Y. Gu, E. Okogbue, H. Chou, J. Shi, Y. Zhang, S.K. Banerjee, Y. Jung, J.C. Lee, D. Akinwande. A Library of Atomically Thin 2D Materials Featuring the Conductive-Point Resistive Switching Phenomenon. Adv. Mater. 33 (2021), 2007792. doi:https://doi.org/10.1002/adma.202007792.

[19]   S.M. Hus, R. Ge, P.-A. Chen, L. Liang, G.E. Donnelly, W. Ko, F. Huang, M.-H. Chiang, A.-P. Li, D. Akinwande. Observation of single-defect memristor in an MoS_2 atomic sheet. Nat. Nanotechnol. 16 (2020), 58–62. doi:10.1038/s41565-020-00789-w.

[20]   F. Pizzocchero, L. Gammelgaard, B.S. Jessen, J.M. Caridad, L. Wang, J. Hone, P. Bøggild, T.J. Booth. The hot pick-up technique for batch assembly of van der Waals heterostructures. Nat. Commun. 7 (2016), 11894. doi:10.1038/ncomms11894.

[21]   I. Lazić, E.G.T. Bosch, S. Lazar. Phase contrast STEM for thin samples: Integrated differential phase contrast. Ultramicroscopy 160 (2016), 265–280. doi:10.1016/j.ultramic.2015.10.011.

[22]   K. Müller, F.F. Krause, A. Béché, M. Schowalter, V. Galioit, S. Löffler, J. Verbeeck, J. Zweck, P. Schattschneider, A. Rosenauer. Atomic electric fields revealed by a quantum mechanical approach to electron picodiffraction. Nat. Commun. 5 (2020), 5653. doi:10.1038/ncomms6653.

[23]   N. Shibata, T. Seki, G. Sánchez-Santolino, S.D. Findlay, Y. Kohno, T. Matsumoto, R. Ishikawa, Y. Ikuhara. Electric field imaging of single atoms. Nat. Commun. 8 (2017), 15631. doi:10.1038/ncomms15631.

[24]   T. Blu, F. Luisier. The SURE-LET Approach to Image Denoising. IEEE Trans. Image Process. 16 (2007), 2778–2786. doi:10.1109/TIP.2007.906002.

[25]   J. Barthel. Dr . Probe: A software for high-resolution STEM image simulation. Ultramicroscopy 193 (2018), 1–11. doi:10.1016/j.ultramic.2018.06.003.

[26]   A. Dal Corso. Projector augmented-wave method: Application to relativistic spin-density functional theory. Phys. Rev. B. 82 (2010), 075116. doi:10.1103/PhysRevB.82.075116.

[27]   P. Giannozzi, S. Baroni, N. Bonini, M. Calandra, R. Car, C. Cavazzoni, D. Ceresoli, G.L. Chiarotti, M. Cococcioni, I. Dabo, A. Dal Corso, S. de Gironcoli, S. Fabris, G. Fratesi, R. Gebauer, U. Gerstmann, C. Gougoussis, A. Kokalj, M. Lazzeri, L. Martin-Samos, N. Marzari, F. Mauri, R. Mazzarello, S. Paolini, A. Pasquarello, L. Paulatto, C. Sbraccia, S. Scandolo, G. Sclauzero, A.P. Seitsonen, A. Smogunov, P. Umari, R.M. Wentzcovitch. QUANTUM ESPRESSO: a modular and open-source software project for quantum simulations of materials. J. Phys.: Condens. Matter 21 (2009), 395502. doi:10.1088/0953-8984/21/39/395502.

[28]   J.P. Perdew, K. Burke, M. Ernzerhof. Generalized Gradient Approximation Made Simple. Phys. Rev. Lett. 77 (1996), 3865–3868. doi:10.1103/PhysRevLett.77.3865.